Polish Polar Research
DOI: 10.24425/ppr.2025.153921

Influence of basal melting on ice surface fracture and glacier retreat: A case study at Pine Island Glacier

Boya Yan[1,2,3] ORCID-0000-0002-6733-9012, Baojun Zhang[1,2]* ORCID-0000-0001-5438-8723, Pei Jiang[1,2] ORCID-0009-0002-7175-6406, Qian Li[1,2] ORCID-0009-0008-2401-805X,Yunsi Wu[1,2] ORCID-0009-0002-4746-1587 and Mingliang Liu[1,2] ORCID-0000-0003-0913-4681

[1] *Chinese Antarctic Center of Surveying and Mapping, Wuhan University, 129 Luoyu Road, Wuhan, Hubei Province, 430079, China*
[2] *Key Laboratory of Polar Environment Monitoring and Public Governance (Wuhan University), 129 Luoyu Road, Wuhan, Hubei Province, 430079, China*
[3] *School of Pharmacy, Hubei University of Chinese Medicine, 188 Tanhualin Road, Wuhan, Hubei Province, 430065, China.*
** corresponding author < bjzhang@whu.edu.cn>*

Running title: Basal melt of ice shelf and ice shelf retreat

Abstract: Pine Island Glacier (PIG) is one of the most dynamic ice streams in West Antarctica, with significant basal melting and ice shelf retreat profoundly influencing its behavior. In this study, through remote sensing imagery and ice flow velocity data, we identified two major retreats of the PIG ice shelf in 2015 and 2018, and notable fluctuations in the ice flow velocities of PIG ice flow from 2013 to 2018. Analysis of CryoSat-2 data revealed that the annual average basal melt rate of the ice shelf peaked at ~14±0.8 m yr–1 in 2016. We conducted simulations using an ice flow model to assess the effects of ice shelf retreat and basal melting. The results showed that the significant acceleration of ice flow on PIG in 2018 was due to the removal of the compressive arch during the 2018 ice shelf retreat, causing large dynamic changes. The deceleration in 2016 was attributed to substantial basal melting, which reduced the longitudinal force and weakened the ice shelf's buttressing force, leading to an acceleration in 2017. Furthermore, extensive basal melting promoted the development of surface fractures on the southern side of the main ice shelf, contributing to the significant retreat observed in 2018. Consequently, a "melting-

fracture-collapse-acceleration" process has been identified, which is supposed to occur in ice shelves with significant basal melting. A sudden decrease in the surface flow velocity of an ice shelf may serve as an early warning for an accelerated rate of mass loss in the ice shelf system.

Keywords: Antarctic, basal melt rate, ice shelf retreat, fracture, ice flow model, ice flow velocity.

Introduction

Ice loss from the Amundsen Sea sector of the West Antarctic Ice Sheet (WAIS) contributes about 7% of the global sea-level rise (Stanton *et al.* 2013). Since at least the 1970s, the Amundsen Sea Embayment of the WAIS has experienced significant acceleration, thinning, and grounding line retreat (Joughin and Padman 2003; Konrad *et al.* 2018; Mouginot *et al.* 2014; Rignot et al. 2014). These changes are correlated with the incursions of relative warm Southern Ocean-sourced Circumpolar Deep Water (CDW) onto the continental shelf (Jacobs *et al.* 2011). Approximately 75% of the WAIS is grounded below sea level, and the large-scale collapse could lead to about 3.3 m of global sea lever rise (Bamber *et al.* 2009, 2018).

Pine Island Glacier (PIG) is one of the largest and most dynamic ice streams in West Antarctica (Shean *et al.* 2017). PIG has experienced more than 100 m of thinning since 1970s, a 70% increase in grounding line ice flux and almost doubled the surface velocity between 1974 and 2013 (Mouginot *et al.* 2014). Its grounding line retreated around 30 km along its centerline between 1992 to 2011 (Rignot *et al.* 2014). Ocean-driven basal melting of the PIG ice shelf triggers its acceleration, thinning, and grounding line retreat (Liu *et al.* 2015), which can reduce ice shelf volume and thus the buttressing capability (De Rydt *et al.* 2021).

From the perspective of the physics of glaciers, the acceleration of the PIG ice shelf is usually explored from the following aspects. The increased basal melt that has reduced its buttressing effect results in the potential dynamically instability of the PIG ice shelf, which will induce the speed up of PIG ice flow (Stanton *et al.* 2013). The retreat of the PIG ice shelf that removes the total "safety band" will yield important dynamic consequences, and that means the increase of ice flow (Fürst *et al.* 2016). Changes in the structural rigidity, i.e., ice damage, further significantly impacted ice flow (Sun and Gudmundsson 2023).

Ice flow models can show the dynamic process of ice shelves and ice sheets in case of ice thickness change, ice shelves and grounding line retreat. Constrained by remotely sensed

data, they showed a strong sensitivity to small perturbations in the grounding line position (Joughin *et al.* 2009). A numerical ice flow model also revealed changes in ice shelf buttressing and grounding-line flux due to localized ice thickness perturbations (Zhang *et al.* 2020c). It also displayed diverse subglacial landscapes and had an impact on ice flow and projected global sea-level rise from ice-sheet loss (Bingham *et al.* 2017).

In this study, we extracted the ice flow velocities of PIG from 2013 to 2018 and identified their abnormal changes from 2015 to 2018, along with several significant ice shelf retreats during this period. To investigate the dynamic changes in the PIG ice shelf between 2015 and 2018, and to explore the potential causes of the large-scale ice shelf retreat in 2018, we conducted a series of ice shelf basal melt experiments and two ice shelf retreat experiments, using an ice flow model. The simulation results revealed the potential causes of the notable acceleration of the PIG ice shelf in 2018 and we analyzed the effects of tensile resistive stress on dry surface fractures by integrating linear elastic fracture mechanics with the ice flow model.

Study area

The PIG is located on West Antarctica and its catchment covers ~ 1.8–2.0 10^5 km^2 (Fig. 1), with annual surface mass balance (SMB) estimates of ~ 68 ± 6 Gt yr^{-1} (Medley *et al.* 2014). The elevation of the PIG catchment ranges from ~ 500 to ~ 2500 m, while the PIG ice shelf is lower than ~ 500 m. Ice flow velocities within the PIG catchment are relatively slow, particularly in areas above 1500 m, where velocities are ~ 10 m yr^{-1}. In contrast, the ice flow velocity on the PIG ice shelf exceeds 4300 m yr^{-1} (Fig. 1B). On the ice shelf, 2–4 km wide shear margins separate the main shelf from the northeast ("North shelf") and southwest ("South shelf") sectors of the PIG ice shelf. Total ice shelf area in recent decades varied from ~ 5500 to ~ 6000 km^2 (Shean *et al.* 2019).

Methods

The retreat of the PIG ice shelf may lead to its increased ice flow velocity (Fürst *et al.* 2016), but following the retreat in 2015, the annual average velocities of the PIG ice shelf did not exhibit significant acceleration from 2016 to 2018. Therefore, we focused on the period from 2015 to 2018, analyzing changes in ice shelf velocities, front positions, and ice thickness, while conducting sensitivity experiments using an ice flow model. Since no grounding line retreat > 30

This article has been accepted for publication in a future issue of *PPRes*, but has not been fully edited. Content may change prior to final publication.

km occurred after the major retreat event in 2011 (Rignot *et al.* 2014), changes in its position were not discussed in this study.

Velocities and front positions. — Apart from remote sensing images, the annual ice flow velocity data was needed in this study. To track the front positions of the PIG ice shelf, we used Landsat-8 images from 2015 to 2018, 002row,113path. The Landsat 8 satellite payload consists of two science instruments: the Operational Land Imager (OLI) and the Thermal Infrared Sensor (TIRS). These two sensors provide seasonal coverage of the global landmass at a spatial resolution of 30 meters (visible, NIR, SWIR); 100 meters (thermal); and 15 meters (panchromatic).

Apart from remote sensing images, the annual ice flow velocity data was needed in this study. We used velocity data from 2013 to 2018 generated with the used of auto-RIFT algorithm (https://its-live.jpl.nasa.gov/; Gardner *et al.* 2018), provided by the NASA MEaSUREs ITS_LIVE project (Gardner *et al.* 2019). The spatial resolution of the data is 240 m, and the temporal resolution of the data is one year.

Ice shelf thickness and basal melt rate. — The changes in the ice shelf thickness and basal melt were important factors in the stability of PIG. In this study, ice shelf surface elevation, ice shelf thickness and basal melt rates were calculated from the latest released the CroySat-2 product (Zhang *et al.* 2023). This dataset is provided by the European Space Agency, and covers the period from July 2010 to December 2018.

The Croysat-2 product was used to get the surface elevation of the PIG ice shelf (Zhang *et al.* 2017):

$$H_{icorr} = H_i - (f(x_i, y_i) + m\Lambda + nbs), i = 1 \dots N \qquad (1)$$

where H_{icorr} is the corrected surface elevation value, i is the counter, N denotes the number of observations within each fitted bin, H_i denotes the surface elevation observation, Λ relates to the satellite heading (assigned a value of 0 or 1 depending upon whether it was acquired on an ascending or a descending pass), m denotes the ascending–descending offset, bs denotes backscatter, $f(x_i, y_i)$ denotes the surface fitting of the topography:

$$f(x_i, y_i) = a_1 x_i + a_2 y_i + a_3 x_i y_i + a_4 x_i^2 + a_5 y_i^2 + a_4 x_i y_i^2 + a_5 x_i y_i^2 + a_8 x_i y_i^2 \quad (2)$$

where x_i and y_i denote the projection coordinated in each bin, $a_{1–8}$ are coefficients of a biquadratic surface model accounting for topography.

After the correction of surface elevation observation, the height above sea level can be calculated:

$$e = H_{icorr} - (H_{madt} + H_{geoid}) \qquad (3)$$

This article has been accepted for publication in a future issue of *PPRes*, but has not been fully edited. Content may change prior to final publication.

where e is ice-shelf elevation above mean sea level (the freeboard), H_{madt} is MADT-H (sea surface height above geoid) from Monthly mean and Climatology Maps of Sea Level Anomalies (https://www.aviso.altimetry.fr/en/data/products/sea-surface-height-products/global/gridded-sea-level-anomalies-mean-and-climatology.html#c10358), and H_{geoid} is the geoidal is from EIGEN-6C4 (Foerste *et al.* 2014).

Ice thickness was inferred from surface elevation using the principle of hydrostatic equilibrium. If ice is in hydrostatic equilibrium, its thickness can be determined as (Griggs and Bamber 2011):

$$Hice_i = \frac{(e-\delta)\rho_w}{\rho_w - \rho_i} \qquad (4)$$

where $Hice_i$ is the equivalent ice thickness, *i.e.*, the thickness of the ice shelf would be if all the ice were at the meteoric ice density, ρ_i. ρ_w is the density of the water column under the ice shelf and δ is the firn density correction, from RACMO2.3 regional climate modelling (Lenaerts *et al.* 2012).

Assuming incompressibility, constant ice density, and column-average velocity $\boldsymbol{u}$, the Eulerian description of mass conservation for a column of ice with ice-equivalent thickness $Hice_i$ can be expressed as follows (Eq. 5):

$$\frac{\partial Hice_i}{\partial t} = -\nabla(Hice_i \boldsymbol{u}) + \dot{a} - \dot{b} \quad (5)$$

where $\dot{a}$ is surface mass balance (meters ice equivalent for time interval dt) and $\dot{b}$ is basal melt rate (meters ice equivalent, defined as positive for melt).

The flux divergence term, $\nabla(Hice_i \boldsymbol{u})$, can be expanded as follows (Eq. 6):

$$\nabla(Hice_i \boldsymbol{u}) = Hice_i(\nabla \boldsymbol{u}) + \boldsymbol{u}(\nabla Hice_i) \quad (6)$$

where $\nabla \boldsymbol{u}$ is the velocity divergence (positive for extension) and $\nabla Hice_i$ is the thickness gradient (Shean *et al.* 2019).

Validation was performed using airborne laser altimetry data from the IceBridge program (https://nsidc.org/icebridge/portal/map). The results indicated that the root mean square error (RMSE) for the surface elevation time series compared to airborne laser altimetry data was 5.79 m with an R-squared (R^2) value of 0.97. For the ice shelf thickness time series compared to ice-penetrating radar observations, the RMSE was 58 m with an R^2 value of 0.95. Overall, the precision of the dataset constructed using satellite altimetry in this study is reliable (Zhang *et al.* 2020a, 2020b, 2022, 2023).

Model experiment. — Ice flow model is a necessary tool in revealing the dynamic mechanism of ice shelf changes. We use the Ice Sheet System Model (ISSM) to perform our

This article has been accepted for publication in a future issue of *PPRes*, but has not been fully edited. Content may change prior to final publication.

numerical experiments (Larour *et al.* 2012). The initialization of the model contained the PIG surface elevation data in 2015 (Zhang *et al.* 2021), the ice shelf thickness data in 2015 (Zhang *et al.* 2023) and the PIG bedrock elevation data from BedMachine Antarctica v2 (Morlighem 2020; Morlighem, *et al.* 2020).

After removing the areas with smaller ice flow speeds, the final selected region for our simulation is shown in the Fig. 2A (Morlighem *et al.* 2010; Seroussi *et al.* 2014). The mesh horizontal resolutions vary from 500 m on the ice shelf to 40 km in the mountainous regions because our target area in the sensitivity experiments is the ice shelf area and small region on the upstream of the grounding line (Fig. 2A). The central line is ~ 170 km in length, with about 95 km upstream of the grounding line and 75 km in the ice shelf region. This ensures that in subsequent experiments, we can capture the flow velocity changes both in the ice shelf area and the catchment area. For the velocity on the central line, the average misfits between the observed velocity in 2015 and the initial simulation is 57 m yr^{-1}, which represents 2% of the average speed on the central line (Fig. 2B), making it a reliable reference initial simulation for the subsequent sensitivity experiments.

Ice flow models. — The most complete ice flow model is the full-Stokes set of equations, which includes the momentum balance and incompressibility equations. The acceleration being negligible, these equations are, respectively:

$$\nabla\sigma + \rho_i \boldsymbol{g} = 0 \quad (7)$$

$$\mathrm{Tr}(\dot{\varepsilon}) = 0 \quad (8)$$

where $\nabla\sigma$ is the divergence vector of the stress tensor, σ, $\mathrm{Tr}(\dot{\varepsilon})$ is the trace of the strain rate tensor, $\dot{\varepsilon}$, ρ_i is the ice density and $\boldsymbol{g}$ the acceleration due to gravity. Ice is treated as an isotropic and incompressible material. The pressures, P, is introduced as a Lagrange multiplier to ensure the incompressibility/continuity Eq. (9). The behavior law of ice is:

$$\sigma' = 2\eta\dot{\varepsilon} \quad (9)$$

where $\sigma' = \sigma + P\boldsymbol{I}$ is the deviatoric stress tensor, $\boldsymbol{I}$ is the identity matrix and η is the effective ice viscosity, which follows a generalized Glen's flow law in ISSM (Glen 1955):

$$\eta = \frac{B}{2\dot{\varepsilon}_e^{\frac{n-1}{n}}} \quad (10)$$

B is the ice hardness, n the Glen's law coefficient (here chosen as n=3 (Cuffey and Paterson 2010)), and $\dot{\varepsilon}_e$ is the effective stress:

$$\dot{\varepsilon}_e = \sqrt{\frac{1}{2}\sum_{i,j}\dot{\varepsilon}_{ij}^2} \quad (11)$$

This article has been accepted for publication in a future issue of *PPRes*, but has not been fully edited. Content may change prior to final publication.

In the Shelf Approximation model (SSA) (MacAyeal 1989), the vertical shear is negligible:

$$\dot{\varepsilon}_{xz} = 0; \quad \dot{\varepsilon}_{yz} = 0 \qquad (12)$$

This assumption reduces the equations to a 2D model, as *ux* and *vy* do not depend on depth z. The vertical velocity is deduced from the horizontal velocities, *ux* and *vy*, using Eq. (8) in SSA.

In this study, we did not investigate the changes in the grounding line, so using SSA is reasonable (Morlighem *et al.* 2010).

Thermal model. — Ice hardness, *B*, is mainly temperature dependent, so we need a thermodynamic model of the ice sheet to calculate its value. The thermal equation is derived from the energy conservation equation. We assume that the ice sheet is in thermal steady state, which leads to:

$$\frac{\partial T}{\partial t} = 0; \quad \boldsymbol{v} \cdot \nabla T = \frac{k_{th}}{\rho_i c} \Delta T + \Phi \qquad (13)$$

T is the ice temperature, *t* is time, $\boldsymbol{v}$ is the velocity vector, k_{th} is the ice thermal conductivity, *c* is the ice heat capacity, Φ is the deformational heating and Δ is the Laplace operator. This equation can be solved using ISSM.

Boundary conditions. — The upper boundary condition of the ice flow model is a stress-free. A friction law is applied at the ice-bedrock interface. The basal drag is modeled following Paterson (1994):

$$v_b \propto N_e^{-q} \tau_b^p \qquad (14)$$

where v_b is the basal velocity magnitude, τ_b is the basal stress magnitude, N_e is the effective pressure on the glacier base, here $N_e = \rho g h$, where h is the height of the glacier above buoyancy. *p* and *q* are friction law exponents.

In ISSM, this friction law is implemented in terms of basal stress, following Budd *et al.* (1979):

$$\tau_b = C_b^2 N_e^r v_b^s \qquad (15)$$

where C_b is the friction coefficient, *r* and *s* are friction law exponents, $r = q/p$, $s = 1/p$ and in the initialization of the model, $q = 1$, $p = 1$.

As the basal friction coefficient is difficult to measure remotely and is critical control on ice dynamic, inversions were used in ISSM. It consists in inferring unknown parameters using additional observations. Here, we used surface velocities in 2015 (Gardner *et al.* 2018) to infer the basal friction coefficient.

This article has been accepted for publication in a future issue of *PPRes*, but has not been fully edited. Content may change prior to final publication.

In the thermal model, the surface temperature is the mean annual air temperature from ERA5 data set in 2015 (Hersbach *et al.* 2023). On grounded ice, we imposed a geothermal heat flux (Maule *et al.* 2005) and a frictional heat flux to $\tau_b v_b$. On the ice shelf, basal drag is zero, thermal modelling is unresolved due to the complexity of ice-ocean interaction, and the ice hardness B is inferred using an independent control method. The ice hardness on the ice shelf is based on the values provided in Cuffey and Paterson (2010) assuming thermal steady state, and is inferred using data assimilation surface velocity on floating ice in ISSM. Ice temperature and hardness are updated at each step during data assimilation of basal friction for consistency (Morlighem *et al.* 2010; Seroussi *et al.* 2014).

Results

Changes in surface ice flow velocities and front positions. — We collected remote sensing images from 2015 to 2018 and selected two time points each year to extract the ice shelf front line. When selecting remote sensing images, we aimed to select images of the PIG ice shelf region with cloud cover < 5%, ensuring that one image was taken near the end of summer each year and another near the beginning of summer. During this period, we identified two significant changes in the ice shelf front position (Fig. 3).

The first occurs in 2015. By November, the ice shelf retreats substantially, compared to its front position in March, indicating a large-scale calving event and the ice shelf front retreat during the time. The second major change occurs in 2018. In February, the front line is roughly in the same position as in November 2015, but by November 2018, a noticeable retreat is observed, suggesting another significant calving event. In contrast, the ice shelf front experiences minor advances and retreats in 2016 and 2017, though these changes are much smaller compared to the events of 2015 and 2018.

We extracted the ice flow velocity results along the central line from 2013 to 2018 (Fig. 2A) and found that the changes in ice flow velocity differ significantly between the ice shelf region and the catchment area (Fig. 4B, C). On the PIG catchment (Fig. 4B), the ice flow velocity in 2018 is notably higher than in other years. Near the grounding line (~ 95 km), the ice flow velocity increases by approximately 70 m yr^{-1} in 2018 compared to 2017, whereas in other years, velocity fluctuations near the grounding line are around 10 m yr^{-1}. At ~ 60 km, the ice flow velocity in 2018 reaches ~ 2500 m yr^{-1}, slightly higher than the 2017 velocity (~ 2480 m yr^{-1}), while in the other years, velocities remain stable at ~ 2450 m yr^{-1} from 2013 to 2016.

This article has been accepted for publication in a future issue of *PPRes*, but has not been fully edited. Content may change prior to final publication.

On the ice shelf, the changes in velocity are more complex (Fig. 4C). From 2013 to 2015, the ice flow velocities on the ice shelf increase steadily, with the maximum velocity rising by ~ 100 m each year. However, in 2016, the velocities along the central line between 110 and 150 km drop significantly compared to 2015. In 2017, the velocities begin to recover. By 2018, the maximum ice flow velocity rises to ~ 4400 m yr^{-1}.

Changes in the ice shelf thickness and basal melt rate. — Based on ice thickness and basal melt data (Zhang *et al.* 2023), we calculated the monthly average equivalent thickness of the ice shelf. The error in the monthly average thickness during the period shown in Fig. 5 is ~ 49 m, which accounts for about 13% of the average ice shelf equivalent thickness over the entire period. Additionally, we calculated the annual average basal melt rate of the ice shelf. The results show a clear correlation between the trend of monthly average thickness changes and the basal melt rates.

As seen in Fig. 5, the 3-month smoothed curve reveals that before January 2016, the monthly average ice thickness fluctuates ~ 390 m. However, from 2016 to 2017, it decreases to ~ 370 m. Although there is a slight increase in ice thickness after 2017, it remains fluctuating ~ 370 m. The basal melt was stable ~ 10 m yr^{-1} till the end of 2013, but it started increasing in 2014, reaching the peak of ~ 14 m yr^{-1} in the middle of 2016. Since then, it is slowly decreasing. The sustained high basal melt rates from 2015 to 2018 lead to the gradual thinning of the ice shelf, with the average thickness after 2017 being ~ 20 meters lower than the average before 2016.

Sensitivity experiment results. — To investigate the fluctuations of the surface velocity on the PIG ice shelf from 2015 to 2018, we conducted several sensitivity experiments to study the dynamic mechanisms driven by basal melt and ice shelf retreat (Table 1 and Fig. 6). Our sensitivity experiments were based on the initial simulation, constrained by some boundary conditions derived from observed data in 2015, in Section Ice Flow Models.

There are two steady state simulations in the retreat experiments. Based on the initial simulation, we changed the external forcing with the ice shelf front lines from the front line 1 to the front line 2. In the “re_1”, the front line 1 is the front position (Fig. 6) referred to the front position in March 2016 (Fig. 3). In the “re_2”, the front line 2 is the front position (Fig. 6) referred to the front position in November 2018 (Fig. 3).

The basal melt experiments include four transient experiments. The front line in the four transient experiments is front line 1. “1yr” simulation is the beginning of the four transient simulations, and the subsequent simulations from “2yr” to “4yr” are performed with the basal

This article has been accepted for publication in a future issue of *PPRes*, but has not been fully edited. Content may change prior to final publication.

melt rate. Due to the significant difference in basal melt rates between the main ice shelf and the two sides, we set the following conditions in the experiment: over the main ice shelf, the basal melt rate is 50 m yr^{-1}, and along the two sides of the shelf, the basal melt rate is 5 m yr^{-1} (Shean *et al.* 2019).

By extracting the surface ice flow velocity along the central line of the PIG ice shelf retreat experiments in Fig. 7A, we find that the two cases of the ice shelf retreat lead to different changes in the ice flow velocity. In the re_1 experiment, the ice shelf retreats by ~ 15 km along the central line, but this does not result in a significant acceleration of the ice shelf flow. However, in the re_2 experiment, although the ice shelf retreats by ~ 20 km along the central line, just ~ 5 km longer than in the re_1 experiment, it causes an increase in the ice flow velocities across the entire central line. These experimental results are consistent with our observations in section "Changes in surface ice flow velocities and front positions".

In Fig. 7B, the results from the basal melt experiments indicate that high basal melt rate of the ice shelf leads to fluctuations in the ice flow velocity. In the transient simulations with substantial basal melting, the ice flow velocities along the central line beyond ~ 110 km are significantly lower in the 2yr experiment compared to the same region velocities in the 1yr experiment, while the velocities on the catchment (< 95 km) show little variation between these two experiments. Under continued basal melting, the 3yr and 4yr experiments show significant increases in ice flow velocities on both the ice shelf and the catchment.

Discussion

Ice shelf retreat and acceleration. — The retreat of the ice shelf front does not necessarily lead to a significant increase in ice flow speed. In ice dynamic studies, the maximum area that can be removed without causing a large increase in ice flow velocity can be estimated by calculating the "compressive arch" (Doake *et al.* 1998) or safety band (Fürst *et al.* 2016). Here, we use the "compressive arch" calculation to explain the changes in ice flow velocity observed in the different retreat experiments, as discussed in section "Sensitivity experiment results".

When calculating and showing the characteristic patterns of a "compressive arch", the key is to invert the distribution of the least principal strain rates field from the surface velocity field of the ice shelf (Doake *et al.* 1998). The least principal strain rates represent the maximum

compression and minimum tension on the ice shelf. The magnitudes of the minimum ($\dot{\varepsilon}_1$) and the maximum ($\dot{\varepsilon}_2$) tensile principal strain rates can be calculated as (Wang *et al.* 2021):

$$\dot{\varepsilon}_1 = \frac{1}{2}\left(\dot{\varepsilon}_{xx} + \dot{\varepsilon}_{yy}\right) - \sqrt{\frac{1}{4}\left(\dot{\varepsilon}_{xx} - \dot{\varepsilon}_{yy}\right)^2 + \dot{\varepsilon}_{xy}^2}$$

$$\dot{\varepsilon}_2 = \frac{1}{2}\left(\dot{\varepsilon}_{xx} + \dot{\varepsilon}_{yy}\right) + \sqrt{\frac{1}{4}\left(\dot{\varepsilon}_{xx} - \dot{\varepsilon}_{yy}\right)^2 + \dot{\varepsilon}_{xy}^2} \qquad (16)$$

$$\theta = \frac{1}{2}\left[arctan\left(\frac{2\dot{\varepsilon}_{xy}}{\dot{\varepsilon}_{xx} - \dot{\varepsilon}_{yy}}\right)\right]$$

where θ is the angle between the y axis and the principal axis of $\dot{\varepsilon}_1$ if $\dot{\varepsilon}_{xx} > \dot{\varepsilon}_{yy}$, or between the y axis and the principal axis of $\dot{\varepsilon}_2$ if $\dot{\varepsilon}_{xx} < \dot{\varepsilon}_{yy}$. The principal axis of $\dot{\varepsilon}_1$ is perpendicular to the principal axis of $\dot{\varepsilon}_2$. The strain rates $\dot{\varepsilon}_{xx}$, $\dot{\varepsilon}_{yy}$, and $\dot{\varepsilon}_{xy}$ are:

$$\dot{\varepsilon}_{xx} = \frac{\partial v}{\partial x}$$

$$\dot{\varepsilon}_{yy} = \frac{\partial v}{\partial y} \qquad (17)$$

$$\dot{\varepsilon}_{xy} = \frac{1}{2}\left(\frac{\partial v}{\partial x} + \frac{\partial v}{\partial y}\right)$$

Based on equations (16) and (17), we calculated the least principal strain rates field for the initial simulation and used the field to plot the "compressive arch" for the initial simulation (Fig. 8). The red lines indicate that the region with $\dot{\varepsilon}_1$ larger than zero is in the stretching region, while the blue lines indicate the region with $\dot{\varepsilon}_1 < 0$ is in the compression region. Therefore, the "compressive arch" is found in the initial simulation. Once the "compressive arch" is removed, important dynamic consequences would appear. This is demonstrated in the sensitivity experiments as follows: in the re_2 experiment, a significant acceleration of PIG occurs, whereas such an acceleration does not occur in the re_1 experiment.

Clearly, in the two retreat experiments, the differences in the ice flow velocity results are related to the positions of the ice shelf front. In the re_1 experiment, the removed portion of the ice shelf is primarily outside the "compressive arch". Removing this part does not cause significant dynamic changes in the ice shelf, and thus, the increases in ice flow velocities in the re_1 experiment are minimal. Whereas, in the re_2 experiment, the removed portion extends beyond the "compressive arch". This leads to substantial dynamic changes in the ice shelf, resulting in a marked acceleration of ice flow velocities along the central line of PIG, as observed in the experimental results. We believe this explanation also applies to the acceleration of the PIG in 2018, as analyzed in section "Changes in surface ice flow velocities and front positions".

This article has been accepted for publication in a future issue of *PPRes*, but has not been fully edited. Content may change prior to final publication.

Changes in longitudinal force in basal melt experiments. — In the basal melt experiments described in section "Sensitivity experiment results", following the basal melting of the ice shelf, the ice flow on PIG does not immediately accelerate. Instead, the ice flow on the PIG ice shelf ice shelf initially decelerates (Fig. 7B, 2yr), followed by an ice flow acceleration along the entire central line of the PIG (Fig. 7B, 3yr and 4yr). Therefore, the deceleration of the ice flow on the ice shelf is not caused by a slowdown in the catchment ice flow. We believe this is due to extensive basal melting of the ice shelf. To explain this phenomenon, we calculated the longitudinal force acting on the ice shelf.

The longitudinal force (F_L) on the ice shelf is obtained by subtracting the forces resisting ice flow, back force (F_B, also called buttressing force), from the driving force (F_D) (Cuffey and Paterson 2010; Zhang *et al.* 2020c). We follow Cuffey and Paterson (2010) and define back force, F_B, as the difference between the driving force of an ice shelf, F_D, and the net longitudinal force pulling the ice shelf outward is:

$$\begin{aligned} F_B &= F_D - F_L \\ F_D &= \frac{1}{2}\rho_i g(1-\frac{\rho_i}{\rho_w})H^2 \\ F_L &= H(2\tau_{xx}^f + \tau_{yy}^f) \end{aligned} \qquad (18)$$

where H is the ice shelf thickness, τ_{xx}^f and τ_{yy}^f are the along-flow and across-flow deviatoric stresses, respectively.

In Fig. 9, we show the changes in the F_L of the ice shelf from the 1yr to the 4yr experiments in the transient simulations. The results indicate that in the 2yr experiment, most areas of the ice shelf experience negative F_L, meaning the forces driving the outward flow of the ice shelf decreased, which causes the deceleration of the ice flow velocities. In the 3yr and 4yr experiments, the F_L in the ice shelf returns to positive values, with the forces generally larger than those in the 1yr experiment. This corresponds with the accelerations of the ice shelf velocities observed in the 3yr and 4yr experiments in section "Sensitivity experiment results". Additionally, the acceleration of the ice flow on the PIG catchment in the 3yr and 4yr experiments (Fig. 7B) also reveals the reduction in F_B, caused by significant thinning of the ice shelf, thus increasing ice flow velocities on the PIG catchment (Stanton *et al.* 2013; Zhang *et al.* 2020c). Accordingly, the hypothetical scenarios and analysis in these experiments can explain the sudden deceleration of the PIG ice shelf velocities in 2016, as described in section "Changes in surface ice flow velocities and front positions".

This article has been accepted for publication in a future issue of *PPRes*, but has not been fully edited. Content may change prior to final publication.

Surface fracture depth from integrating linear elastic fracture mechanics. — Several stresses affect the depth of a surface fracture, and tensile resistive stress associated with large-scale ice-shelf flow acts to open the fracture (Lai *et al.* 2020). As the integrating linear elastic fracture mechanics (LEFM) is coupled with ice flow model in this research, Weertman's solution (Weertman 1973) was used to calculate the theoretical depth of dry surface fractures in the basal melt experiments.

Background tensile resistive stress (van der Veen and Whillans 1989), R_{xx}, associated with large-scale ice shelf flow acts to open the fracture. Here

$$R_{xx} = 4\eta\dot{\varepsilon}_{xx} \quad (19)$$

and we coupled LEFM with the ice flow model, using

$$d_s = \frac{\pi R_{xx}}{2\rho_i g} \quad (20)$$

to determine the surface fracture depth d_s (Weertman's solution).

Figure 10 shows the changes in dry surface fracture depths in the basal melt experiments. Since the retreat of the PIG ice shelf occurs at its front, we marked the main ice shelf front with a black rectangle for easier reference in subsequent discussions. On the left side of the rectangle, the fracture depths remain stable at ~ 40 meters from 1yr to 4yr experiments. In the center of the rectangle, the fractures are relatively shallow, ranging from 0 to 20 m. However, on the right side of the rectangle, corresponding to the southern front of the main ice shelf, significant changes in the fracture depth are observed. In the 1yr experiment, the fracture depths at the southern edge exceed 30 m. In the 2yr experiment, the area with fracture depths > 30 m expands. In the 3yr and 4yr experiments, although the extent of the fracture zone > 30 m at the front decreases, the upstream region experiences an increase in fracture depths > 30 m, extending toward the southern front of the main ice shelf.

The fluctuations in the theoretical depths of dry surface fractures induced instability at the southern front of the main ice shelf, which aligns with the findings of a fracture study by Liu *et al.* (2022). In the basal melt experiments, the extensive basal melting of the ice shelf leads to the formation of fractures at the southern front, and the subsequent increases in ice flow velocities further accelerate the fractures development in this region. As the observation (Liu *et al.* 2022), a significant fracture appeared at the southern front of the ice shelf in 2018, ultimately triggering a major retreat of the ice shelf. Clearly, this indicates that our experimental results are consistent with the observations as significant basal melting may lead to the development of fractures at the ice shelf front, which in turn contributes to the retreat of the ice shelf.

This article has been accepted for publication in a future issue of *PPRes*, but has not been fully edited. Content may change prior to final publication.

The ice shelf velocity and the stability of the ice shelf system. — The risk of accelerated mass loss from an ice shelf and its catchment, hereafter referred to as the ice shelf system, is a crucial factor in assessing the stability of an ice shelf system (Bell and Seroussi 2020; Dawson *et al.* 2022). Since ice shelves serve as the primary outlets for mass loss from catchments and buttress the ice sheet, previous studies have focused on investigating the frequency of ice shelf calving, retreat of ice shelves, and changes in basal melt rates (Joughin and MacAyeal 2005; Depoorter *et al.* 2013; Liu *et al.* 2015). These factors have been key approaches for exploring the stability of the ice shelf system. However, evaluating the stability of an ice shelf and its catchment solely from an observational perspective is not compelling, as it only provides insight into the current changes and trends within an ice shelf system.

Through sensitivity experiments on PIG in this study, we explain, from the physics of glaciers perspective, the potential changes in the ice shelf system caused by basal melting and the retreat of the ice shelf. In the retreat experiments, we discovered that there are regions at the ice shelf front where removal does not lead to an increase in the ice flow velocities. However, when the retreat of the ice shelf front exceeds the extent of the "compressive arch", both the ice shelf and the upstream catchment experience a significant acceleration in ice flow, which in turn results in an increased rate of mass loss from the ice shelf system. This confirms that the stability of the ice shelf system is highly sensitive to the retreat of the ice shelf.

In the basal melt experiments, we find that a decrease in ice shelf flow velocity does not necessarily indicate an increase in the stability of the ice shelf system. Moreover, significant melting at the ice shelf bottom may initially cause a slowdown in the ice flow speed. However, in the following years, both the ice shelf and the upstream catchment may experience a significant acceleration, resulting in ice flow velocities much higher than those prior to the melting. Furthermore, the dynamic processes induced by basal melting could lead to the formation of new surface fractures or the deepening of existing ones in certain areas at the ice shelf front, potentially triggering ice shelf calving event, or retreat. Once the ice shelf retreat exceeds the original extent of the "compressive arch", it will further accelerate the ice flow in the ice shelf system.

In summary, a "melting-fracture-collapse-acceleration" process has been demonstrated through our sensitivity experiments. This process is not unique to PIG but can also occur in other Antarctic ice shelves. Particularly in the Amundsen Sea, where basal melt rates are high (Zhang *et al.* 2020b, 2023), a sudden decrease in ice shelf surface velocities could serve as an early warning for subsequent acceleration in an ice shelf system mass loss.

This article has been accepted for publication in a future issue of *PPRes*, but has not been fully edited. Content may change prior to final publication.

Conclusions

Using the remote sensing imagery, we extracted the PIG ice shelf front positions from 2015 to 2018. Combined with ice flow velocity data, this study summarized the ice flow velocity variations of the PIG from 2013 to 2018. Between 2015 and 2018, two significant retreats of the PIG ice shelf were observed, one in 2015 and another in 2018. From 2013 to 2016, the ice flow velocities on the PIG catchment remained stable, but in 2017, the velocities increased, and by 2018, a significant acceleration was observed. From 2013 to 2015, the ice flow velocities of the PIG ice shelf increased annually, but in 2016, they decreased compared to 2015. In 2017, the ice flow velocities recovered, culminating in a notable acceleration by 2018.

We analyzed the ice thickness and basal melt rates of the PIG ice shelf from 2010 to 2018. The PIG ice shelf experienced a notable thinning trend between 2016 and 2017, with ice thickness fluctuating ~ 390 m before 2016 and stabilizing ~ 370 m after 2017. The basal melt rate mirrored the changes in ice thickness, peaking at 2016 at ~ 14±0.8 m yr^{-1}.

With an ice flow model combined with the "compressive arch" theory, longitudinal force analysis, and LEFM for the theoretical depth of dry surface fractures, we explained the fluctuations in the ice flow velocity from 2015 to 2018 and the significant retreat of the ice shelf in 2018. The decrease in ice flow velocities from 2015 to 2016 was caused by substantial basal melting, which reduced the longitudinal force (F_L) in the ice shelf. The increase in ice flow velocities from 2016 to 2018 was related to the rapid replenishment to the ice shelf by ice from the PIG catchment, which restored the F_L. The overall acceleration of PIG ice flow in 2018 was linked to the removal of the "compressive arch" during the 2018 ice shelf retreat, leading to significant dynamic changes in the ice shelf. Furthermore, the extensive basal melting in 2016, which accelerated the fracture development on the southern side of the main ice shelf, ultimately led to the collapse and large-scale retreat of the ice shelf in 2018.

Through the analysis of PIG observational and sensitivity experiment results, we identified a "melting-fracture-collapse-acceleration" process, which is of significant relevance to ice shelves with intense basal melting. Particularly in the Amundsen Sea, where basal melting is severe, a decrease in ice shelf surface velocity may not necessarily indicate that the ice shelf system is stabilizing. On the contrary, this could serve as an early warning for an accelerated rate of mass loss in the future.

This article has been accepted for publication in a future issue of *PPRes*, but has not been fully edited. Content may change prior to final publication.

Data Statement. — The velocity data (https://its-live.jpl.nasa.gov/) were generated using auto-RIFTand provided by the NASA MEaSUREs ITS_LIVE project. The Pine Island Glacier surface elevation data were from https://doi.org/10.11888/Glacio.tpdc.271665. The ice shelf thickness data were from https://doi.org/10.11888/Cryos.tpdc.300850. MADT products were processed by SSALTO/DUACS and distributed by AVISO+ (https://www.aviso.altimetry.fr) with support from CNES. Sea surface height above geoid is the data from the Ssalto/Duacs altimeter products, produced and distributed by the Copernicus Marine and Environment Monitoring Service (CMEMS) (https://marine.copernicus.eu/). The Landsat 8 data can be down loaded via the link: https://earthexplorer.usgs.gov/, from Landsat Collection 2 Level-1 data set. The CroySat-2 dataset was provided by the European Space Agency (https://earth.esa.int/eogateway/catalog/cryosat-products). ISSM is the result of a collaboration between the Jet Propulsion Laboratory and University of California at Irvine (https://issm.jpl.nasa.gov/).

Acknowledgements. — This research was supported by the Natural Science Foundation of Hubei Province of China (2023AFB591), Key Laboratory of Polar Environment Monitoring and Public Governance (Wuhan University), Ministry of Education (202306), and the Fundamental Research Funds for the Central Universities (2042024kf0016, 2042022dx0001). We thank the reviewers for their comments.

References

Bamber J.L., Riva R.E.M., Vermeersen B.L.A. and LeBrocq A.M. 2009. Reassessment of the potential sea-level rise from a collapse of the West Antarctic Ice Sheet. *Science* 324: 901–903. doi: 10.1126/science.1169335

Bamber J.L., Westaway R.M., Marzeion B. and Wouters B. 2018. The land ice contribution to sea level during the satellite era. *Environmental Research Letters* 13: 063008. doi: 10.1088/1748-9326/aac2f0

Bell R.E. and Seroussi H. 2020. History, mass loss, structure, and dynamic behavior of the Antarctic Ice Sheet. *Science* 367: 1321–1325. doi: 10.1126/science.aaz5489

Bingham R.G., Vaughan D.G., King E.C., Davies D., Cornford S.L., Smith A.M., Arthern R.J., Brisbourne A.M., De Rydt J., Graham A.G.C., Spagnolo M., Marsh O.J. and Shean D.E. 2017. Diverse landscapes beneath Pine Island Glacier influence ice flow. *Nature Communications* 8: 1618. doi: 10.1038/s41467-017-01597-y

Budd W., Keage P. and Blundy N. 1979. Empirical studies of ice sliding. *Journal of Glaciology* 23: 157–170. doi: 10.3189/S0022143000029804

Cuffey K.M. and Paterson W.S.B. 2010. *The physics of glaciers*. Elsevier, Burlington, MA, 4th edition.

Dawson E.J., Schroeder D.M., Chu W.N., Mantelli E. and Seroussi H. 2022. Ice mass loss sensitivity to the Antarctic Ice Sheet basal thermal state. *Nature Communications* 13: 4957. doi: 10.1038/s41467-022-32632-2

De Rydt J., Reese R., Paolo F.S. and Gudmundsson G.H. 2021. Drivers of Pine Island Glacier speed-up between 1996 and 2016. *The Cryosphere* 15: 113–132. doi: 10.5194/tc-15-113-2021

Depoorter M.A., Bamber J.L., Griggs J.A., Lenaerts J.T.M., Ligtenberg S.R.M., van den Broeke M.R. and Moholdt G. 2013. Calving fluxes and basal melt rates of Antarctic ice shelves. *Nature* 502: 89–92. doi: 10.1038/nature12567

Doake C.S.M., Corr H.F.J., Rott H., Skvarca P. and Young N.W. 1998. Breakup and conditions for stability of the northern Larsen Ice Shelf, Antarctica. *Nature* 391: 778–780. doi: 10.1038/35832

Foerste C., Bruinsma S.L., Abrykosov O., Lemoine J., Marty J.C., Flechtner F., Balmino G., Barthelmes F. and Biancale R. 2014. EIGEN-6C4. The latest combined global gravity field model including GOCE data up to degree and order 2190 of GFZ Potsdam and GRGS Toulouse. GFZ Data Services. doi: 10.5880/icgem.2015.1

Fürst J.J., Durand G., Gillet-Chaulet F., Tavard L., Rankl M., Braun M. and Gagliardini O. 2016. The safety band of Antarctic ice shelves. *Nature Climate Change* 6: 479–482. doi: 10.1038/nclimate2912

Gardner A.S., Moholdt G., Scambos T., Fahnstock M., Ligtenberg S., van den Broeke, M. and Nilsson J. 2018. Increased West Antarctic and unchanged East Antarctic ice discharge over the last 7 years. *The Cryosphere* 12: 521–547. doi: 10.5194/tc-12-521-2018

Gardner A.S., Fahnestock M.A. and Scambos T.A. 2019. [update to time of data download]: MEaSUREs ITS_LIVE Landsat Image-Pair Glacier and Ice Sheet Surface Velocities: Version 1. Data archived at National Snow and Ice Data Center. doi: 10.5067/IMR9D3PEI28U

Glen J.W. 1955. The creep of polycrystalline ice. *Proceedings of the Royal Society of London. Series A. Mathematical and Physical Sciences* 228: 519–538. doi:10.1098/rspa.1955.0066

Griggs J.A. and Bamber J.L. 2011. Antarctic ice-shelf thickness from satellite radar altimetry. *Journal of Glaciology* 57: 485–498. doi: 10.3189/002214311796905659

Hersbach H., Bell B., Berrisford P., Biavati G., Horányi A., Muñoz Sabater J., Nicolas J., Peubey C., Radu R., Rozum I., Schepers D., Simmons A., Soci C., Dee D. and Thépaut J-N. 2023. ERA5 hourly data on single levels from 1940 to present. Copernicus Climate Change Service (C3S) Climate Data Store (CDS). doi :10.24381/cds.adbb2d47

Jacobs S.S., Jenkins A., Giulivi C.F. and Dutrieux P. 2011. Stronger ocean circulation and increased melting under Pine Island Glacier ice shelf. *Nature Geoscience* 4: 519–523. doi:10.1038/ngeo1188

Joughin I. and MacAyeal D.R. 2005. Calving of large tabular icebergs from ice shelf rift systems. *Geophysical Research Letters* 32: L02501. doi: 10.1029/2004gl020978

Joughin I. and Padman L. 2003. Melting and freezing beneath Filchner-Ronne Ice Shelf, Antarctica. *Geophysical Research Letters* 30: 1477. doi: 10.1029/2003gl016941

Joughin I., Tulaczyk S., Bamber J.L., Blankenship D., Holt J.W., Scambos T. and Vaughan D.G. 2009. Basal conditions for Pine Island and Thwaites Glaciers, West Antarctica, determined using satellite and airborne data. *Journal of Glaciology* 55: 245–257. doi: 10.3189/002214309788608705

Konrad H., Shepherd A., Gilbert L., Hogg A.E., McMillan M., Muir A. and Slater T. 2018. Net retreat of Antarctic glacier grounding lines. *Nature Geoscience* 11: 258–262. doi: 10.1038/s41561-018-0082-z

Lai C.Y., Kingslake J., Wearing M.G., Chen P.H.C., Gentine P., Li H., Spergel J.J. and van Wessem J.M. 2020. Vulnerability of Antarctica's ice shelves to meltwater-driven fracture. *Nature* 584: 574–578. doi: 10.1038/s41586-020-2627-8

Larour E., Seroussi H., Morlighem M. and Rignot E. 2012. Continental scale, high order, high spatial resolution, ice sheet modeling using the Ice Sheet System Model (ISSM). *Journal of Geophysical Research-Earth Surface* 117: F01022. doi: 10.1029/2011jf002140

Lenaerts J.T.M., van den Broeke M.R., van de Berg W.J., van Meijgaard E. and Munneke P.K. 2012. A new, high-resolution surface mass balance map of Antarctica (1979–2010) based on regional atmospheric climate modeling. *Geophysical Research Letters* 39: L04501. doi: 10.1029/2011gl050713

Liu S., Su S., Cheng Y., Tong X. and Li R. 2022. Long-term monitoring and change analysis of Pine Island Ice Shelf based on multi-source satellite observations during 1973–2020. *Journal of Marine Science and Engineering* 10: 976. doi: 10.3390/jmse10070976

Liu Y., Moore J. C., Cheng X., Gladstone R.M., Bassis J.N., Liu H., Wen J. and Hui F. 2015. Ocean-driven thinning enhances iceberg calving and retreat of Antarctic ice shelves. *Proceedings of the National Academy of Sciences of the United States of America* 112: 3263–3268. doi: 10.1073/pnas.1415137112

MacAyeal D.R. 1989. Large-scale ice flow over a viscous basal sediment - theory and application to ice stream-b, Antarctica. *Journal of Geophysical Research-Solid Earth and Planets* 94: 4071–4087. doi: 10.1029/JB094iB04p04071

Maule C.F., Purucker M.E., Olsen N. and Mosegaard K. 2005. Heat flux anomalies in Antarctica revealed by satellite magnetic data. *Science* 309: 464–467. doi :10.1126/science.1106888

Medley B., Joughin I., Smith B.E., Das S.B., Steig E.J., Conway H., Gogineni S., Lewis C., Criscitiello A.S., McConnell J.R., van den Broeke M.R., Lenaerts J.T.M., Bromwich D.H., Nicolas J.P. and Leuschen C. 2014. Constraining the recent mass balance of Pine Island and Thwaites glaciers, West Antarctica, with airborne observations of snow accumulation. *The Cryosphere* 8: 1375–1392. doi: 10.5194/tc-8-1375-2014

This article has been accepted for publication in a future issue of *PPRes*, but has not been fully edited. Content may change prior to final publication.

Morlighem M. 2020. MEaSUREs BedMachine Antarctica, Version 2. Boulder, Colorado USA. NASA National Snow and Ice Data Center Distributed Active Archive Center. doi: 10.5067/E1QL9HFQ7A8M

Morlighem M., Rignot E., Seroussi H., Larour E., Ben Dhia H. and Aubry D. 2010. Spatial patterns of basal drag inferred using control methods from a full-Stokes and simpler models for Pine Island Glacier, West Antarctica. *Geophysical Research Letters* 37: L14502. doi: 10.1029/2010gl043853

Morlighem M., Rignot E., Binder T., Blankenship D., Drews R., Eagles G., Eisen O., Ferraccioli F., Forsberg R., Fretwell P., Goel V., Greenbaum J.S., Gudmundsson H., Guo J.X., Helm V., Hofstede C., Howat I., Humbert A., Jokat W., Karlsson N.B., Lee W.S., Matsuoka K., Millan R., Mouginot J., Paden J., Pattyn F., Roberts J., Rosier S., Ruppel A., Seroussi H., Smith E.C., Steinhage D., Sun B., van den Broeke M.R., van Ommen T.D., van Wessem M. and Young D.A. 2020. Deep glacial troughs and stabilizing ridges unveiled beneath the margins of the Antarctic ice sheet. *Nature Geoscience* 13: 132–137. doi: 10.1038/s41561-019-0510-8

Mouginot J., Rignot E. and Scheuchl B. 2014. Sustained increase in ice discharge from the Amundsen Sea Embayment, West Antarctica, from1973 to 2013. *Geophysical Research Letters* 41: 1576–1584. doi: 10.1002/2013gl059069

Paterson W. 1994. *The physics of glaciers*. Pergamon, Oxford, 3rd edition.

Rignot E., Mouginot J., Morlighem M., Seroussi H. and Scheuchl B. 2014. Widespread, rapid grounding line retreat of Pine Island, Thwaites, Smith, and Kohler glaciers, West Antarctica, from 1992 to 2011. *Geophysical Research Letters* 41: 3502–3509. doi: 10.1002/2014gl060140

Seroussi H., Morlighem M., Rignot E., Mouginot J., Larour E., Schodlok M. and Khazendar A. 2014. Sensitivity of the dynamics of Pine Island Glacier, West Antarctica, to climate forcing for the next 50 years. *Cryosphere* 8: 1699–1710. doi: 10.5194/tc-8-1699-2014

Shean D.E., Christianson K., Larson K.M., Ligtenberg S.R.M., Joughin I.R., Smith B.E., Stevens C.M., Bushuk M. and Holland D.M. 2017. GPS-derived estimates of surface mass balance and ocean-induced basal melt for Pine Island Glacier ice shelf, Antarctica. *Cryosphere* 11: 2655–2674. doi: 10.5194/tc-11-2655-2017

Shean D.E., Joughin I.R., Dutrieux P., Smith B.E. and Berthier E. 2019. Ice shelf basal melt rates from a high-resolution digital elevation model (DEM) record for Pine Island Glacier, Antarctica. *Cryosphere* 13: 2633–2656. doi: 10.5194/tc-13-2633-2019

Stanton T.P., Shaw W.J., Truffer M., Corr H.F.J., Peters L.E., Riverman K.L., Bindschadler R., Holland D.M. and Anandakrishnan S. 2013. Channelized ice melting in the ocean boundary layer beneath Pine Island Glacier, Antarctica. *Science* 341: 1236–1239. doi: 10.1126/science.1239373

This article has been accepted for publication in a future issue of *PPRes*, but has not been fully edited. Content may change prior to final publication.

Sun S. and Gudmundsson G.H. 2023. The speedup of Pine Island Ice Shelf between 2017 and 2020: revaluating the importance of ice damage. *Journal of Glaciology* 69: 1983–1991. doi: 10.1017/jog.2023.76

van der Veen C.J. and Whillans I. 1989. Force budget: I. Theory and numerical methods. *Journal of Glaciology* 35: 53–60. doi: 10.3189/002214389793701581

Wang S., Alexander P., Wu Q., Tedesco M. and Shu S. 2021. Characterization of ice shelf fracture features using ICESat-2-A case study over the Amery Ice Shelf. *Remote Sensing of Environment* 255: 112266. doi: 10.1016/j.rse.2020.112266

Weertman J. 1973. Can a water-filled crevasse reach the bottom surface of a glacier? Union Géodésique et Géophysique Internatinale. Association Intemationale d'Hydrologie Scientifique. Commission de Neiges et Glaces. *Symposium on the Hydrology of Glaciers, Cambridge* 95: 139–145.

Zhang B., Wang Z., An J. and Liu Y. 2017. Mass change of the Antarctic Ice Sheet inferred from ICESat and CryoSat-2. *Advanced in Polar Science* 28: 185–195. doi: 10.13679/j.advps.2017.3.00185

Zhang B., Wang Z., Yang Q., Liu J., An J., Li F., Liu T. and Geng H. 2020a. Elevation changes of the Antarctic Ice Sheet from joint Envisat and CryoSat-2 radar altimetry. *Remote Sensing* 12: 3746. doi: 10.3390/rs12223746

Zhang B., Liu J., Wang Z., Liu T. and Yang Q. 2020b. Antarctic ice-shelf thickness changes from CryoSat-2 SARIn mode measurements: Assessment and comparison with IceBridge and ICESat. *Journal of Earth System Science* 129: 127. doi: 10.1007/s12040-020-01392-2

Zhang B., Wang Z., Yang Q., Liu J., An J., Li F. and Geng H. 2021. Surface elevation time series of Antarctic ice sheet (2002–2019). National Tibetan Plateau/Third Pole Environment Data Center. doi: 10.11888/Glacio.tpdc.271665

Zhang B., Wang Z., An J., Liu T. and Geng H. 2022. A 30-year monthly 5 km gridded surface elevation time series for the Greenland Ice Sheet from multiple satellite radar altimeters. *Earth System Science Data* 14: 973–989. doi: 10.5194/essd-14-973-2022

Zhang B., Wang Z., An J., Yan B., Liu M. and Wu S. 2023. Antarctic ice shelves surface elevation, thickness and basal mass balance (1991–2020). National Tibetan Plateau/Third Pole Environment Data Center. doi: 10.11888/Cryos.tpdc.300850

Zhang T., Price S.F., Hoffman M.J., Perego M. and Asay-Davis X. 2020c. Diagnosing the sensitivity of grounding-line flux to changes in sub-ice-shelf melting. *Cryosphere* 14: 3407–3424. doi: 10.5194/tc-14-3407-2020

Received 23 September 2024

Accepted 8 March 2025

Table 1.

The sensitivity experiments conducted in the study.

Experiment type	Name	Simulation type	Changes in external forcing
Retreat experiment	re_1	Steady	Front line 1
	re_2		Front line 2
Basal melt experiment	1yr	Transient	Front line 1
	2yr		Front line 1; Basal melt 50 m yr^{-1} on the main ice shelf; Basal melt 5 yr^{-1} on the two sides of the ice shelf
	3yr		
	4yr		

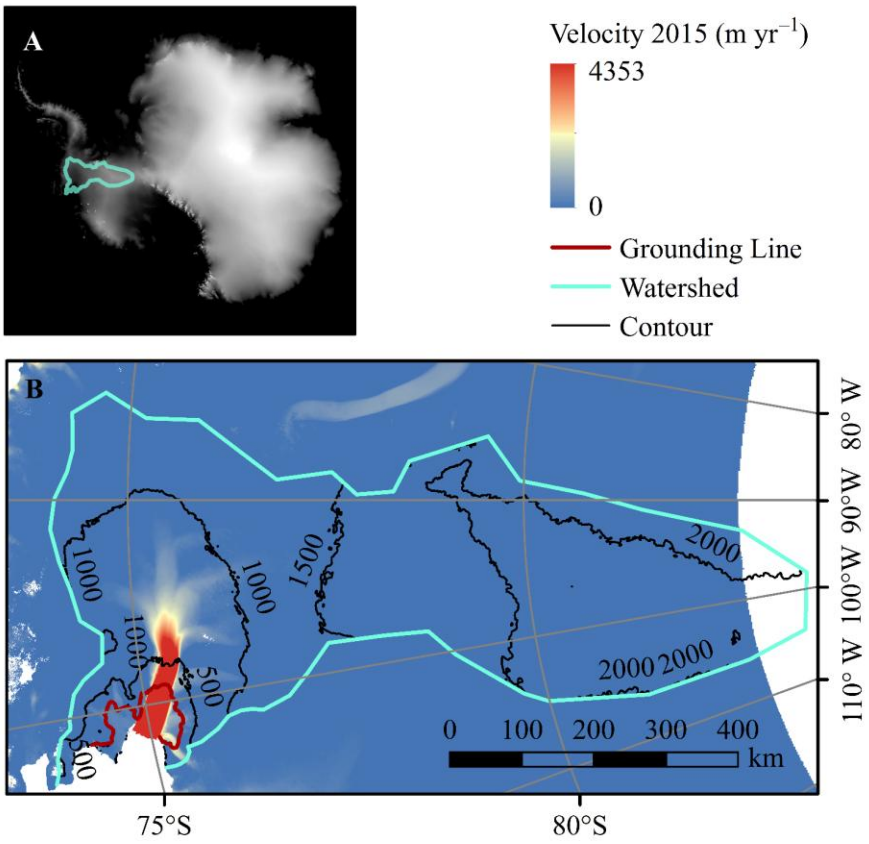

Fig. 1. Geographic Setting of PIG. (**A**) PIG location on the West Antarctica. (**B**) The PIG ice shelf and its catchment. The velocity data is from Gardner *et al.* (2018). The surface elevation in 2015 and the grounding line data are referred to Zhang *et al.* (2020a, 2021).

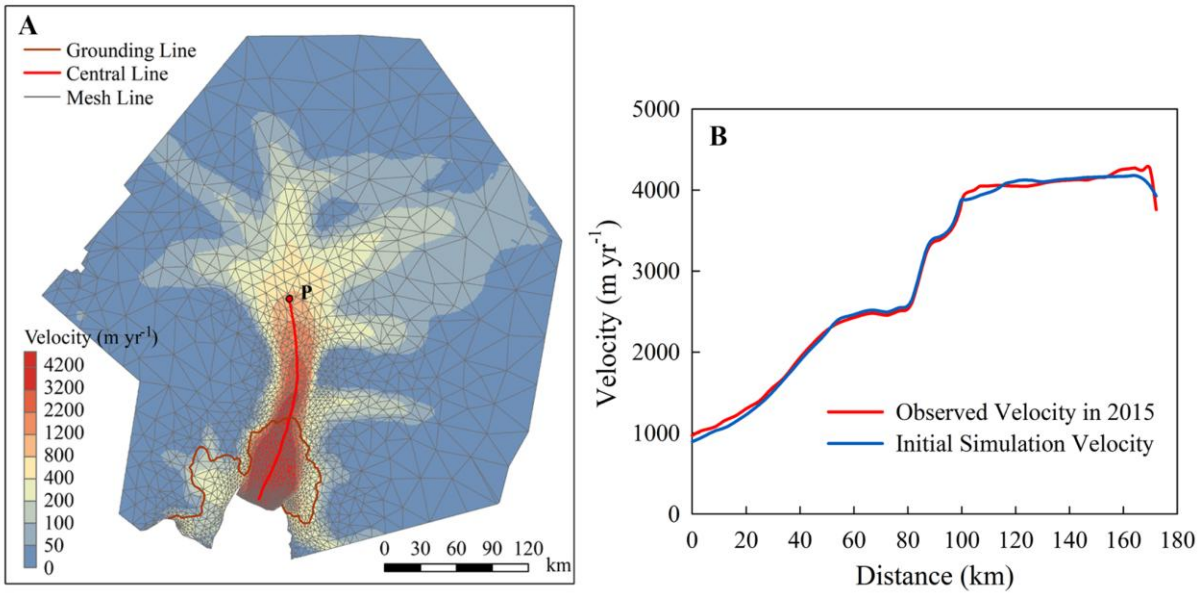

Fig. 2. Initial Simulation. (**A**) Mesh lines and simulated surface velocity of PIG. Point P is the beginning of the central line; (**B**) The observed velocity in 2015 (Gardner *et al*. 2018) and the initial simulation velocity along the central line.

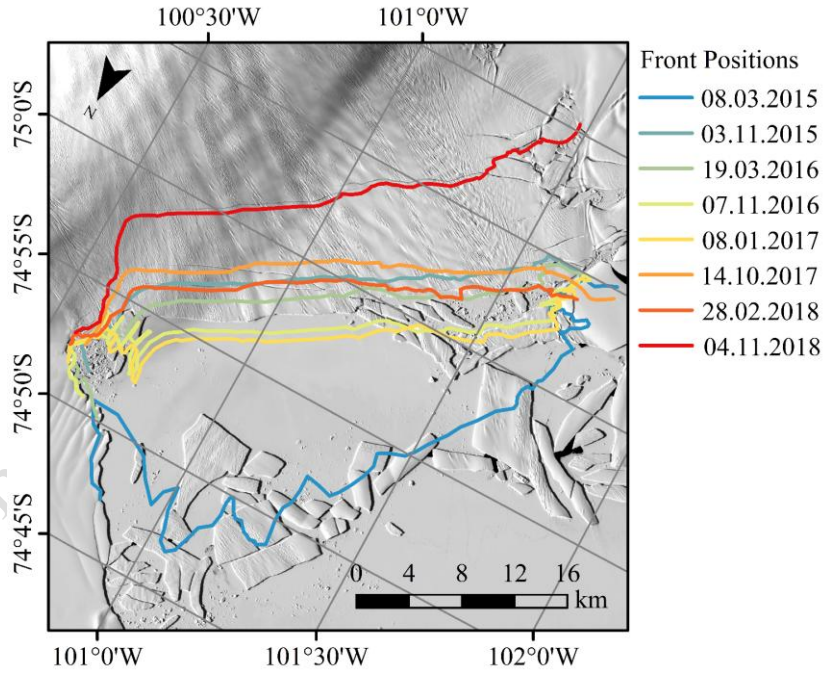

Fig. 3. The ice shelf front positions of the PIG ice shelf from 08.03.2015 to 04.11.2018 according to the Lansat-8 images. The background is from Landsat-8, 2018.10.1, 002row,113path.

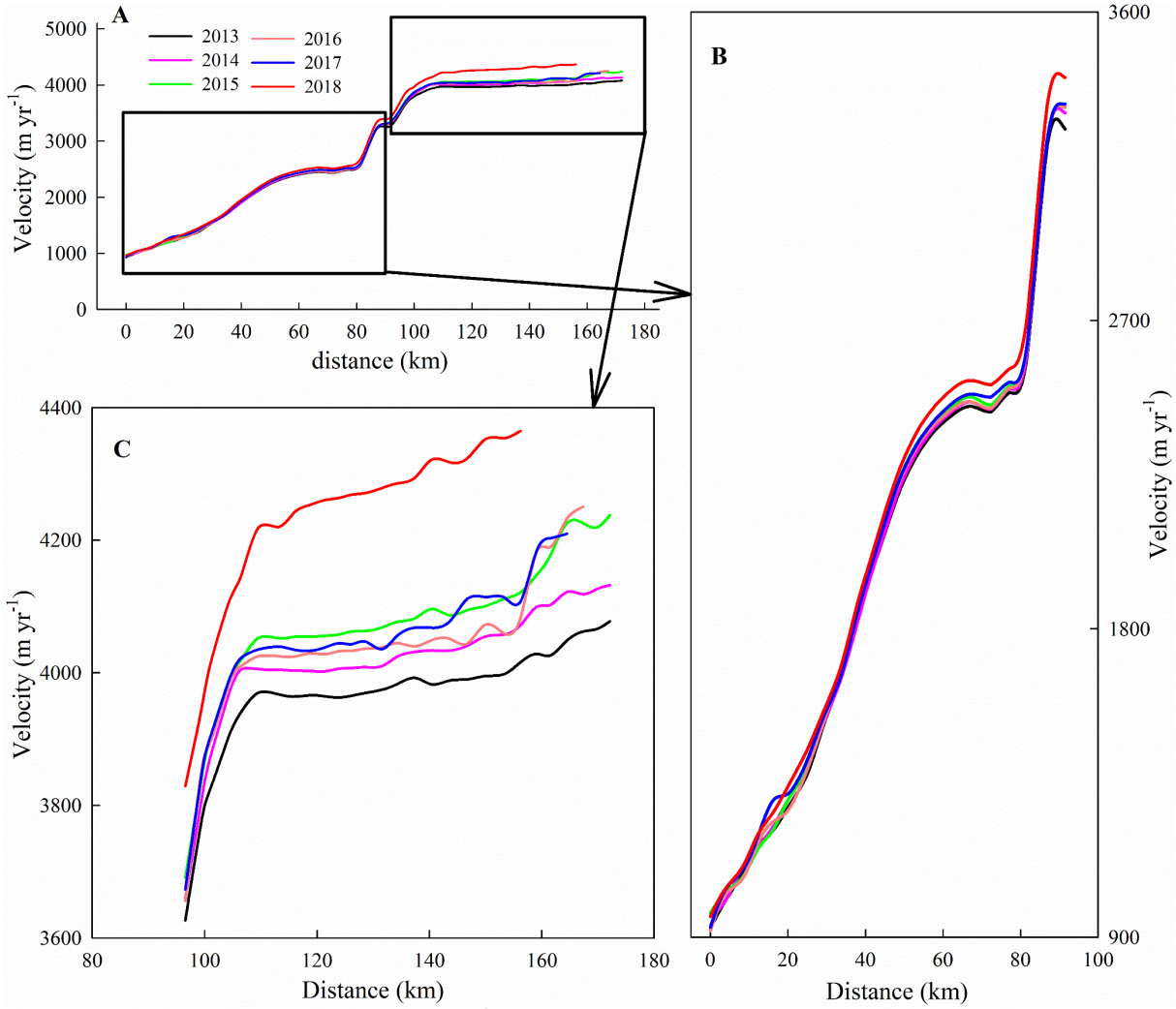

Fig. 4. PIG surface velocities from 2013 to 2018 on the central line according to Fig. 2A. (**A**) The surface velocities along the central line from point P, (**B**) the surface velocities on the PIG ice shelf on the catchment (upstream grounding line), along the central line, and (**C**) the surface velocities on the PIG ice shelf along the central line.

This article has been accepted for publication in a future issue of *PPRes*, but has not been fully edited. Content may change prior to final publication.

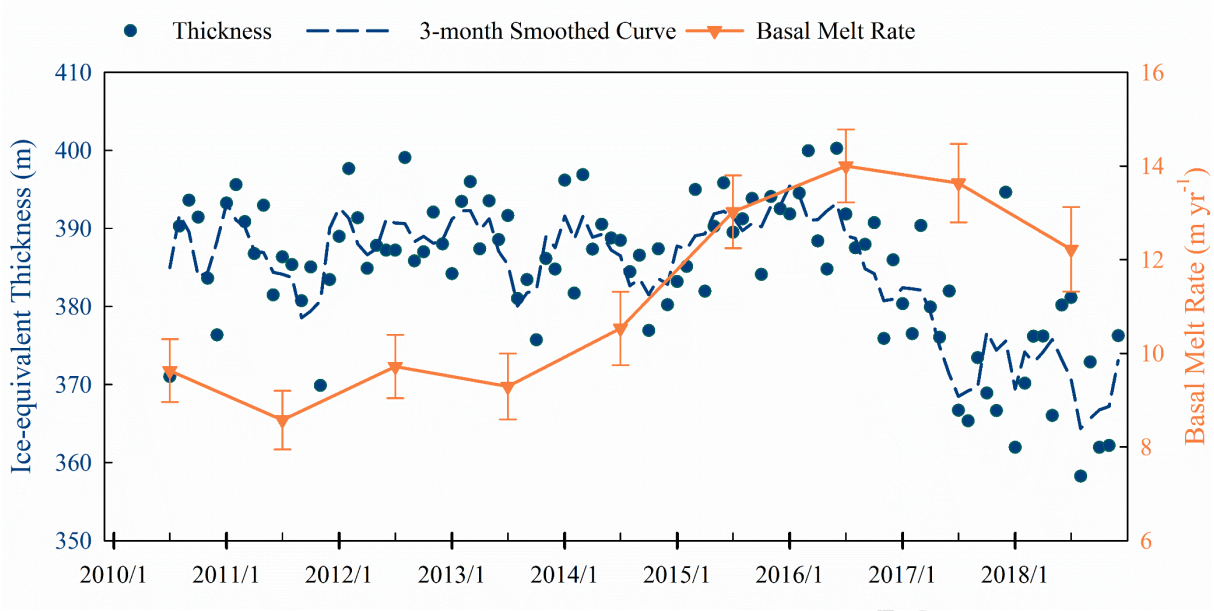

Fig. 5. The monthly average ice equivalent thickness of the PIG ice shelf and the annual ice shelf basal melt rate based on the CroySat-2 product.

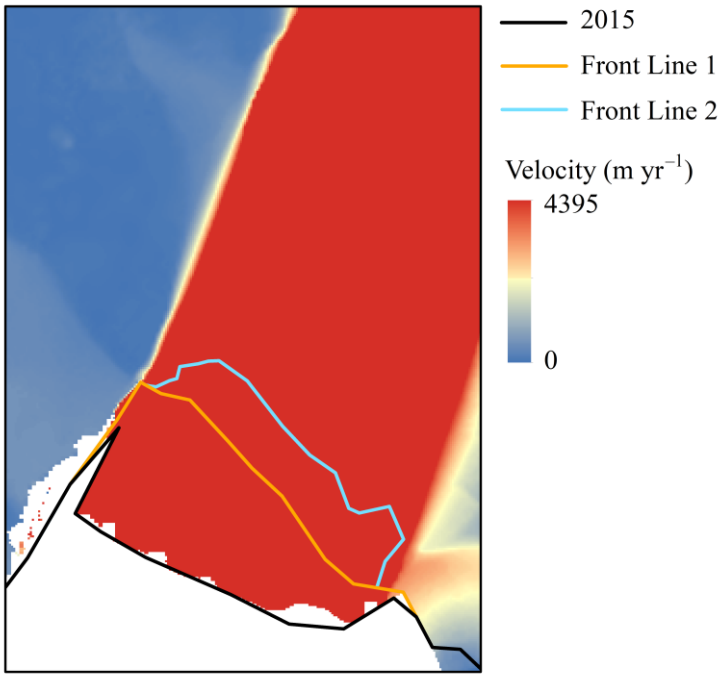

Fig. 6. The PIG ice shelf front positions in the initial simulation and the sensitivity experiments. The black line "2015" is the front position in the initial simulation. The front line 1 and front line 2 are referred to the front positions in Fig. 3 on 19.03.2016 and 04.11.2018, respectively.

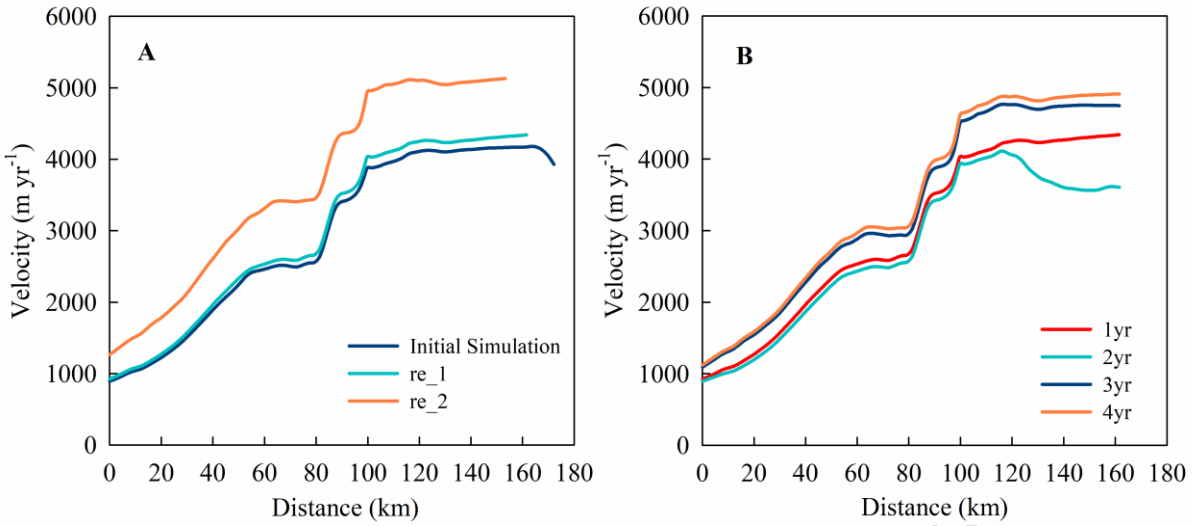

Fig. 7. The velocities along the central line in different experiments: (**A**) Retreat experiments velocities (re_1, re_2), initial model velocities (2015) and (**B**) velocities along the central line in 4 basal melt experiments.

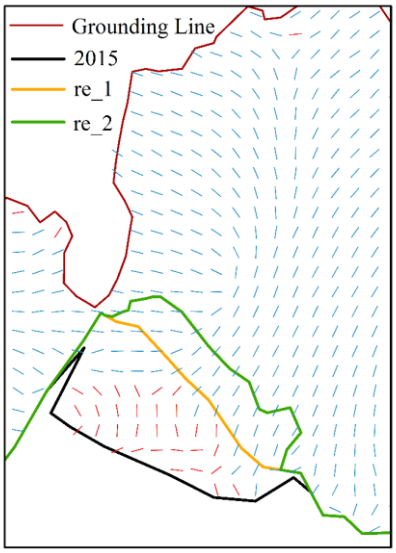

Fig. 8. The strain-rate trajectories ($\dot{\varepsilon}_1$) for the ice-front configuration. The red lines indicate that the region with $\dot{\varepsilon}_1 > 0$ was in the stretching region, while the blue lines indicate that the region with $\dot{\varepsilon}_1 < 0$ was in the compression region. The green line, yellow line and black line indicate area the front positions in the two retreat experiments and the initial simulation respectively.

This article has been accepted for publication in a future issue of *PPRes*, but has not been fully edited. Content may change prior to final publication.

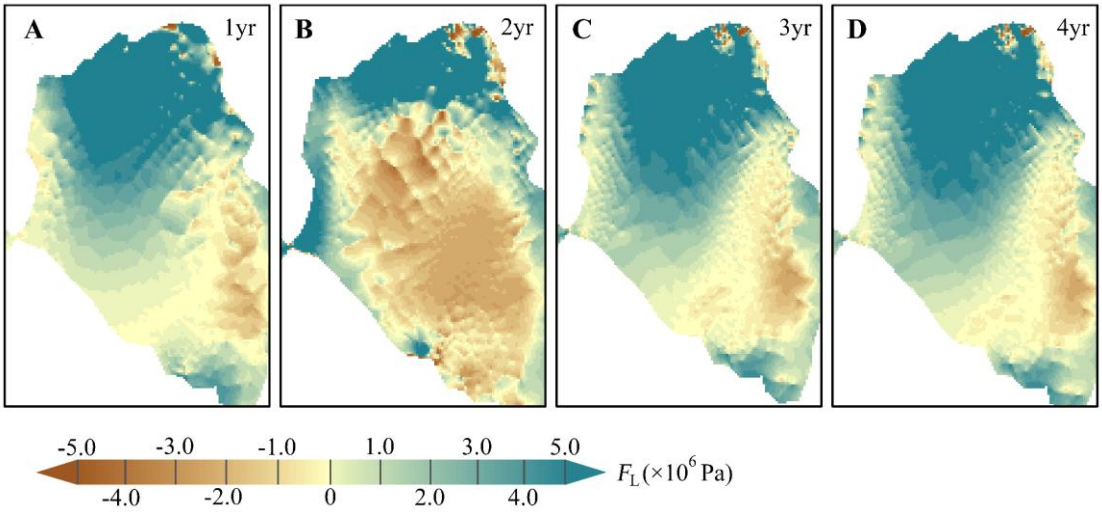

Fig. 9. Longitudinal force (F_L) of the PIG ice shelf in the basal melt experiments. Panels **A** to **D** display the distribution of F_L in the basal melt experiments from "1yr" to "4yr".

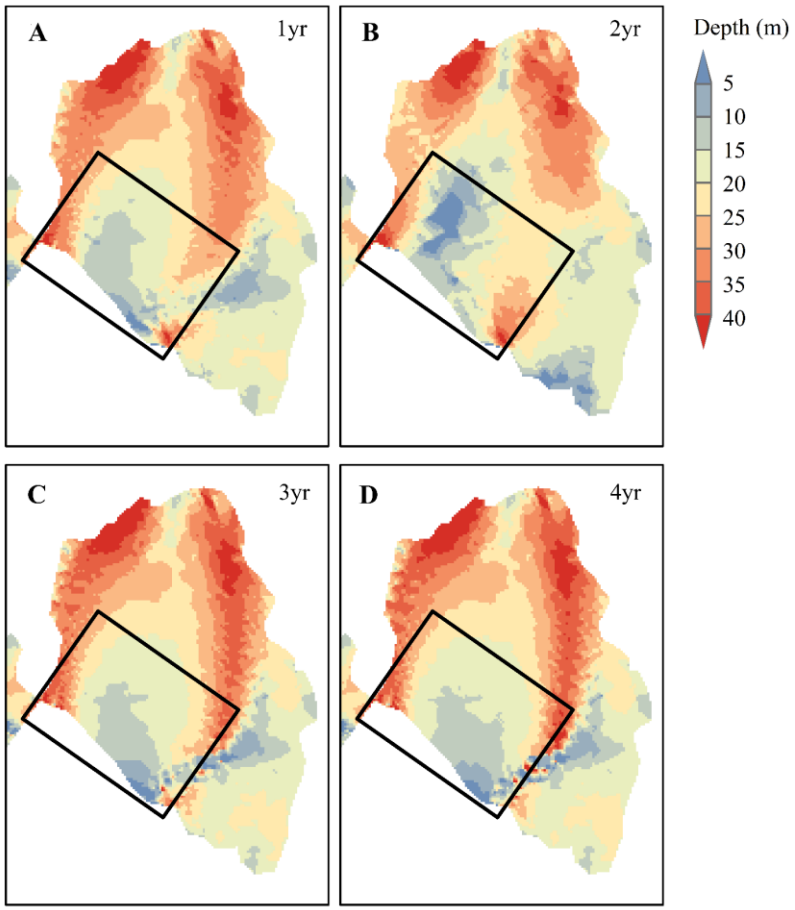

Fig. 10. Depth of dry surface fractures on the PIG ice shelf. Panels **A** to **D** display the distribution of dry surface fracture depth in the basal melt experiments. The black rectangle marks the ice shelf front of the main shelf.